CrossMark

Multi-epoch L-band Spectroscopy of the Be Star μ Centauri Prior to Outburst

G. Aguayo[1] , R. E. Mennickent[1], A. Granada[2,4,5], and S. Otero[3]

[1] Universidad de Concepción Departamento de Astronomía Casilla 160-C, Concepción, Chile; gusaguayo@astro-udec.cl
[2] Department of Physics and Astronomy, The University of Western Ontario, Canada
[3] Buenos Aires, Argentina American Association of Variable Star Observers (AAVSO) Cambridge, MA, USA

Abstract

With the aim of contributing to the understanding of the disk formation process in Be stars, we pursued a one-year spectroscopic observing campaign of the Be star μ Centauri in the L-band, using VLT/ISAAC. We present the nine near-IR spectra we obtained in an epoch of relative photometric quiescence prior to an outburst of $\Delta V = 0.4$ magnitude. Visual estimates during the epoch of our L-band spectroscopy are also presented for the first time, together with the unpublished complete visual light curve between the years 1998 and 2014. We observe significant and monotonic changes in emission line strength of Bracket-α and Pfund-γ lines relative to Humphreys lines, and also in the continuum slope. We interpret these observed changes in terms of important changes to the column density of the line emitting regions, moving from an optically thin to an optically thick stage just prior to a major outburst. For each observing date, we provide estimates for the column density and relative extension of the line emitting region. If the changes observed toward the end of our observing campaign were related to mass-loss changes from the central star, they would correspond to an increase in a factor of two in the mass of the disk in the innermost region. If related to the visual outburst observed one month later, the variability observed in our spectra would be the first detection of the early disk formation process in the L-band.

Key words: circumstellar matter – infrared: stars – stars: emission-line, Be – stars: mass-loss

Supporting material: machine-readable table

1. Introduction

Be stars are well known for being fast rotators, in many cases reaching velocities close to the break-up velocity (e.g., Townsend et al. 2004; Frémat et al. 2005; Martayan et al. 2007). Be stars are broadly known as B-type non-supergiant stars that show, or have shown during their lifetimes, emission in the Hα line (Jaschek et al. 1981). This emission is formed by hydrogen ionization and posterior electron recombination in a circumstellar gaseous envelope ($n_e \sim 10^{12}\,\mathrm{cm}^{-3}$) that has been ejected from the star by an as yet unknown mechanism. Most Be stars have variable brightness over a wide variety of timescales from hours to years, which reflects different physical processes occurring in the star and its surrounding environment. In particular, mass ejection from the central star is responsible for long-term variability, and the transient nature of the Be phenomenon is given by the formation and possible dissipation of the disk.

The origin of the mechanisms involved in the appearance of the Be phenomenon has challenged astrophysicists for 150 years, since the first observation of γ Cas by Jesuit father Secchi in 1867. In past decades, the Be phenomenon has been reviewed in two major pieces of work, by Porter & Rivinius (2003) and more recently by Rivinius et al. (2013).

Polarimetric data and optical interferometric observations support the hypothesis of a geometrically flattened circumstellar disk with $H/R \sim 0.1$ and $\rho/\rho_0 \sim r^{-n}$ with $n \approx 3.5$, where ρ_0 is the disk central density and, H and R the disk height and radius, respectively (Rivinius et al. 2013 and references therein). An important observational insight into the behavior of mass ejection and envelope formation/dissipation comes from the identification of loops in the color–magnitude diagram

of some outbursting Be stars (de Wit et al. 2006). These loops were modeled with an optically thick disk ejected by the star that posteriorly dissipates as an optically thin ring. This feature in the color–magnitude diagram, already noted by Dougherty et al. (1994) has been explored more recently by Haubois et al. (2012). These authors interpret this loop in terms of the different timescales of the build-up and dissipation of the disk, that is, the timescale for disk formation is shorter than the dissipation timescale. Similar conclusions were obtained by Vieira et al. (2017). A correlation between Hα emission and visual magnitude strength has been proposed by Harmanec (1983) and more recently supported by Sigut & Patel (2013), who interpreted the correlation in terms of disks that grow in size and/or density with time. The Be star outbursts are presently being modeled within the theory of viscous decretion disks controlled by variable mass loss $\dot{M}$ and parameterized through the viscosity parameter α (Haubois et al. 2012; Rímulo et al. 2015).

Lee et al. (1991) constructed a viscous, geometrically thin Keplerian disk to describe the circumstellar environment of Be stars. These disks were assumed to be similar to accretion disks but with the angular momentum being supplied at the inner boundary by an uncertain mechanism, and carried away with the matter drifting outwards through the action of viscosity. This scenario became successful in describing the observed characteristics in Be stars mentioned above and has been developed since then by Porter (1999), Bjorkman (1997), Okazaki et al. (2002), Bjorkman & Carciofi (2005), Carciofi et al. (2012), Haubois et al. (2014), Draper et al. (2014), and Vieira et al. (2017) among others.

The results obtained with the viscous decretion disk model suggest that the process of mass ejection and subsequent envelope development can affect the behavior of emission line decrements, in particular in the infrared spectral region. While

---

[4] Now at Instituto de Astrofsica de La Plata CCT La Plata, CONICET-UNLP, Paseo del Bosque S/N B1900FWA La Plata, Argentina.
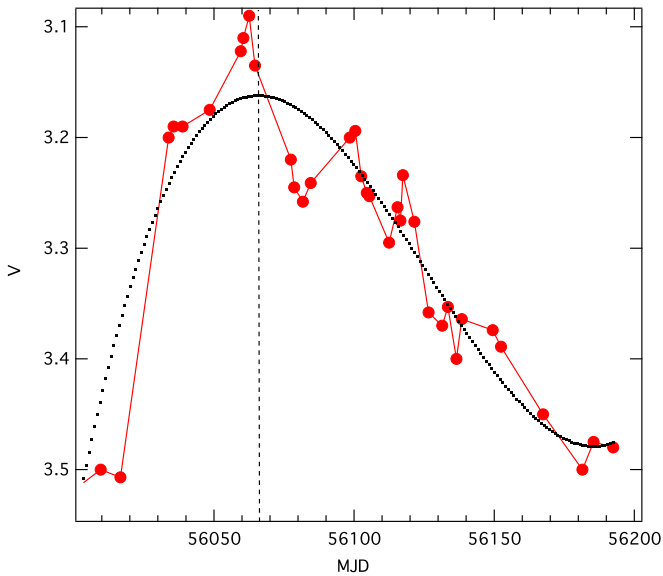[5] Creator of AASTeX v6.1.

Figure 1. Outburst of μ Centauri with a peak at MJD = 56066.6. The red curve corresponds to Argelander photometry and the dotted curve is the fit using a fifth-degree polynomial. The black dashed vertical line represents the maximum intensity of the peak.

optical lines (specially Hα) probe the external disk regions (e.g., Haubois et al. 2014), near-infrared hydrogen lines are much better tracers for the inner parts of the disk.

However, only in recent years has the near-IR region of the spectrum been studied in greater detail. The Apache Point Observatory Galactic Evolution Experiment (APOGEE) allowed for the identification of a large number of new Be stars among objects originally targeted as telluric standard stars, with high-resolution (R = 22,500) H-band spectroscopy (Chojnowski et al. 2015). The variability of these Be stars was studied in a follow-up article (Chojnowski et al. 2017) and by Labadie-Bartz et al. (2017).

The L-band of the near-IR (2.9–4.1 μm) has neither been studied with the same resolution nor for the same amount of targets as the H-band, but it has provided an excellent tool to study the environment of Be stars. The L-band contains important diagnostic Hydrogen lines of Bracket series (Brα, Brβ), Pfund series (Pfγ), and also the Humphreys series, which yield kinematical and physical information of the innermost circumstellar environment, closest to the central star (Marlborough et al. 1997; Lenorzer et al. 2002a, 2002b; Mennickent et al. 2009; Granada et al. 2010). Lenorzer et al. (2002a) presented a line ratio diagram to test the density and spatial distribution of circumstellar gas around hot stars, and as proposed by Jones et al. (2009) and Mennickent et al. (2009), this method can be applied in particular to Be stars.

Thus, studying the time evolution of near-IR L-band lines that form in the innermost region of the disk is of particular interest to understand the formation and dissipation processes observed in Be stars. Sabogal et al. (2017) presented new L-band spectra of a number of Be stars and studied the long-term variability of these objects plus others available in the literature. They found some objects exhibiting disk dissipation, but none exhibiting disk formation. To our knowledge, the process of disk formation has never been observed yet in the L-band.

With the aim of observing a star in the disk formation process in the L-band, we pursued an observational campaign with the aim of tracing the formation, evolution, and dissipation

of the disk of a Be star through near-IR spectroscopy. We decided to choose an early-type Be star, because observations carried out in the optical range have shown that these objects tend to present more recurrent outbursts than late-type objects and are hence more proactive to display the Be phenomenon (Rivinius et al. 2013) and references therein.

The non-radially pulsating Be star μ Centauri (B2Vnpe, $v \sin i = 194\,\mathrm{km\,s}^{-1}$, HD 120324 = HR 5193) was selected due to its brightness ($V \approx 3.45$) and short recurrence time of relatively well documented outbursts (Rivinius et al. 1998a, 1998b, 2001). Particularly for μ Centauri, Hanuschik et al. (1993) studied the circumstellar emission variation in Hα region for a period of about 200 days, finding typical risings of 2–5 days. A few years later, Rivinius et al. (1998a) described the behavior of the stellar and circumstellar activity in this star, finding discrete events characterized as outbursts and concluding that μ Centauri was building a disk that was not detected between 1977 and 1989.

Our original goal was to observe this variable object during a major outburst in order to document the evolution of the physical conditions of the envelope. Surprisingly, we found the star during a rare long quiescence stage, but more surprisingly, we detected important changes in emission line strength prior to a major outburst, which are discussed in this paper.

This paper is organized as follows: in Section 2, we present our observations, the unpublished visual observations of μ Centauri between the years 1998 and 2014, and our photometric and near-IR spectroscopic observations, methodology of spectral reduction, and analysis. In Section 3, we present the main results about line parameters and light curve analysis. We discuss and interpret these results in Section 4. Finally, we present our conclusions in Section 5.

2. Observations

2.1. Photometric Observations

We present for the first time a total of 906 visual magnitudes of μ Centauri distributed from 1998 to 2014. Visual photometry was performed by Sebastián Otero from Buenos Aires, Argentina using the Argelander method (Argelander 1843), which consists of the observation of a target star and non-variable stars as comparison stars with magnitudes and colors as similar as possible to the variable star. This observational method has been recently validated for bright variable stars (Štefl et al. 2003; Carciofi et al. 2012; Chesneau et al. 2014) and results compared with photoelectric photometry with a resulting accuracy of 0.05 mag or better for bright naked eye stars like μ Centauri (Otero et al. 2001; Otero & Moon 2006); we also have compared an outburst centered at MJD = 56066.6 (Figure 1) with the results obtained by Haubois et al. (2012).

In the case of μ Centauri, the availability of suitable comparison stars near the variable contributes to the reliability of the estimates. However, several of the comparison stars used, including the main one, ν Cen, which is only 47 arc minutes away, are variable at the 0.01–0.03 mag. level so this will contribute some scatter to the results. The estimates at the beginning and end of each season—especially before 2004, denoted as a vertical line in Figure 2—may suffer from atmospheric extinction, but over the last several years that effect has been minimized by the use of comparison stars lying at the same altitude of the variable and by averaging estimates using different comparison stars when the conditions were not ideal. This improvement to the observation method was
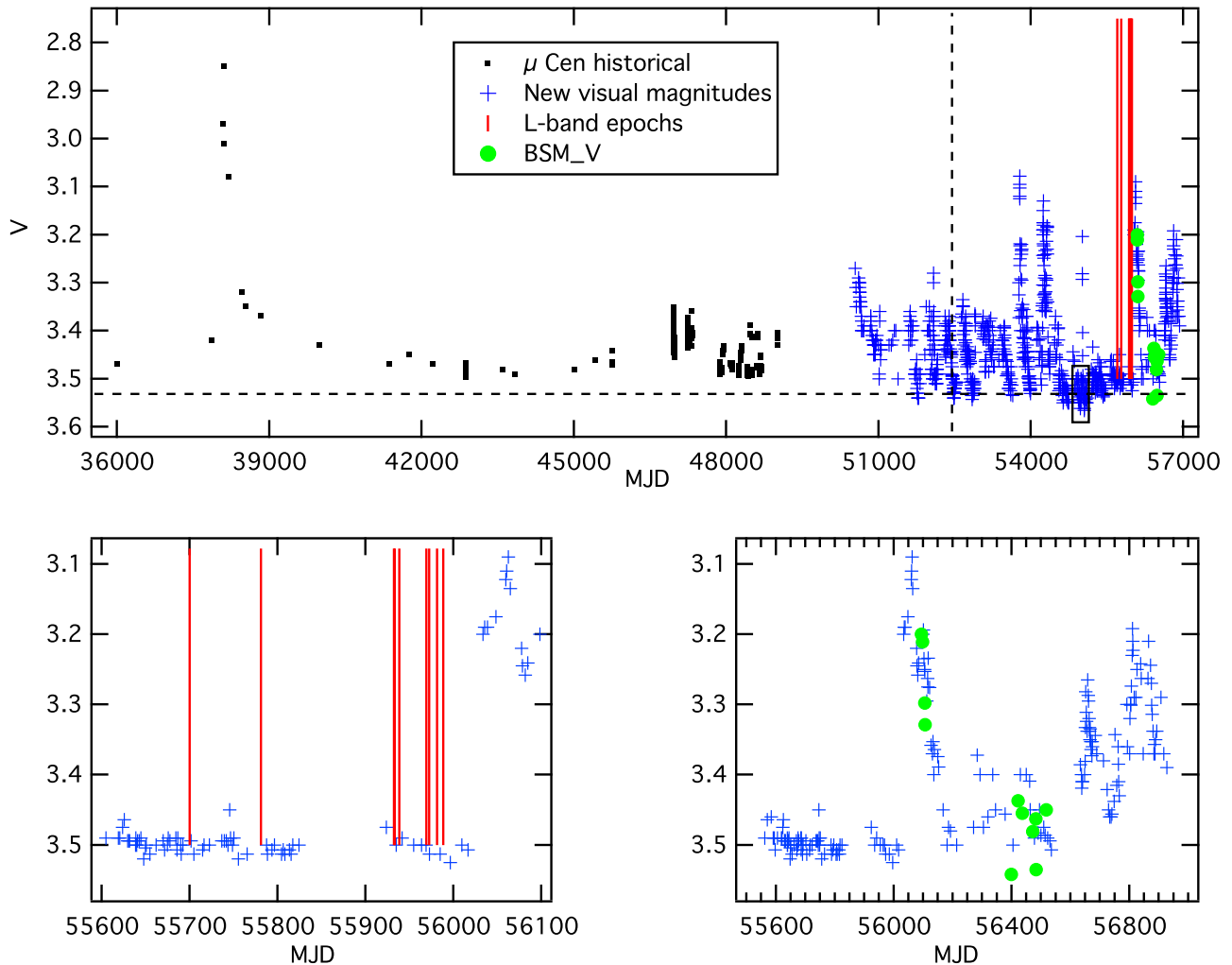
Figure 2. Top panel: light curve of μ Centauri in the V band. The year 2004 is represented by the vertical line. Black dots: historical light curve compiled from different authors (Mendoza 1958; Feinstein 1968, 1975; Gutierrez-Moreno & Moreno 1968; Percy et al. 1981; Stagg 1987; Dachs et al. 1988; Cuypers et al. 1989; Perryman et al. 1997) Blue crosses: visual observations from S. Otero using Argelander method; Red lines: epochs of our L-band spectra; Green circles: BSM photometry used for comparison with visual magnitudes. Dashed line represent historical minimum of μ Cen; this was estimated by averaging the magnitudes within the box with a resulting value of 3.53 mag. Bottom left: a zoom of historical light curve showing the correspondence between L-band epochs and visual photometry. Bottom right: zoom of the historical light curve showing the correspondence between BSM and Argelander photometry.

performed after 2004 and allowed us to maintain the accuracy mentioned above. Even then, only the early epochs were accurate enough to detect the presence of outbursts.

The high variability of μ Centauri due to changes in the disk and color of the star does not affect our visual measurements significantly. Comparison with simultaneous AAVSO BSM Epoch Photometry Data (A. Henden 2018, private communication—Figure 2) confirms that the accuracy is better than 0.05 mag. The comparison stars used are the same for all epochs and are listed in Table 1, and observing log is presented in Table 2. We use the correspondence between the V-band magnitude and our visual magnitudes based on comparison with photoelectric BSO[6] photometry presented in Table 3 and previous studies indicating compatibility between the corresponding data sets as presented in Otero et al. (2001).

2.2. Near-IR Spectroscopic Observations

We obtained nine L-band spectra of μ Centauri using the Infrared Spectrometer and Array Camera (ISAAC;

Table 1
Comparison Stars Used for the Visual Photometric Estimates of μ Centauri Reported in This Paper

Star	V	$B-V$	Comment
λCen	3.13	−0.05	no comment
κ Cen	3.14	−0.21	β Cep, ampl. 0.01 mag.
ν Cen	3.41	−0.23	β Cep, ampl. 0.02 mag.
α Cir	3.18	0.25	roAp, ampl. 0.02 mag.
δ Lup	3.22	−0.22	β Cep, ampl. 0.03 mag.
ϵ Lup	3.37	−0.18	β Cep, ampl. 0.02 mag.
ι Lup	3.55	−0.18	possible β Cep, ampl. 0.01 mag.
β Mus	3.05	−0.19	no comment

Moorwood et al. 1998) located at UT-3 in Cerro Paranal ESO Observatory. Our observations span 10 months from 2011 May 18 to 2012 March 1; the used spectra is shown in Figure 3. The same configuration was used for each spectrum by applying the nodding and chopping observing mode with a central wavelength of 3.55 μm and a narrow slit of 0″3 providing a resolving power $R \approx 1200$. The exposure time of

Table 2
Observing Log for μ Cen and the Telluric Standard HR 4903

Object	MJD	Exptime (s)	Airmass	S/N
μCen	55699.9891	1.848	1.114	133.6
HR 4903	55700.0172	1.848	1.331	⋯
μ Cen	55781.0428	1.848	1.471	127.4
HR 4903	55781.0412	1.848	1.459	⋯
μ Cen	55932.3567	1.848	1.312	137.2
HR 4903	55932.3434	1.848	1.216	⋯
μ Cen	55933.3129	1.848	1.594	95.2
HR 4903	55933.2738	1.848	1.606	⋯
μ Cen	55938.3051	1.848	1.543	125.3
HR 4903	55938.2948	1.848	1.359	⋯
μ Cen	55969.3290	1.848	1.087	122.5
HR 4903	55969.3156	1.848	1.070	⋯
μ Cen	55972.3378	1.848	1.066	131.7
HR 4903	55972.3216	1.848	1.063	⋯
μ Cen	55981.2482	1.848	1.205	137.1
HR 4903	55981.2592	1.848	1.091	⋯
μ Cen	55988.3589	1.848	1.067	139.1
HR 4903	55988.3706	1.848	1.166	⋯

each spectrum was set to 1.8 s providing a signal-to-noise ratio (S/N) larger than 120 in regions deployed of telluric lines.

2.3. Data Reduction

The data were reduced using the ISAAC pipeline and Gasgano software. After reduction process, the images were telluric-corrected using the IRAF[7] telluric task and the standard star HR 4903 observed at similar airmass few minutes before μ Cen. Our telluric standard is HR 4903 of spectral type G1V; this star was divided by a solar spectrum of similar spectral resolution. This reduction process is described by Maiolino et al. (1996). Flux losses due to the narrow slit and seeing variations were large and prevented us from performing a correct calibration of the stellar flux, even considering differential spectrophotometry between μ Centauri and its telluric star. The wavelength calibration allows to identify lines and determine emission line properties, but at the resolving power of $R \sim 1200$, the radial velocities are not quite accurate. For the above reasons, we decided to continuum normalize the spectra and provide information of emission line widths, equivalent widths, relative intensities, and line flux ratios. The analysis and discussion described in this paper is based on these measurements.

3. Results

3.1. Light Curve

We present an up-to-date visual light curve of μ Centauri in Figure 2. The light curve of μ Centauri has been studied by Harmanec (1987), who found a single period of 3.535 days. A few years later, Cuypers et al. (1989) observed the star over two years (1987 and 1988) and used photometric data of 27 nights to find a double-wave light curve with periodicity of 2.1 days using Fourier periodogram analysis. Then, with data taken in 1988, it was possible to refine the period to 2.1017 days. Balona et al. (2001)

also studied μ Centauri photometrically and concluded a periodicity of the order of 1 day; the result of a single period was attributed to co-rotating clouds around the central star. On the contrary, Rivinius et al. (1998a) reported the presence of six periods in μ Cen. Until now, it is clear that there has not been a well established periodicity for this star. Our visual observations are not accurate enough to perform the analysis of small amplitude non-radial pulsation frequencies. However, the visual inspection of our light curve reveals the presence of several outbursts during the last 16 years, which are well above any reasonable estimate for a single point photometric error (Figure 2). In addition to the very large outburst around MJD = 37500, we have found four major outbursts occurring around MJD 53782, 54243, 55014, and 56062; the time lapses between consecutive outbursts are 461, 771, and 1048 days, incompatible with a single recurrence time. The outburst are characterized by a sudden rise of brightness of amplitudes between 0.1 and 0.4 mag, occurring in timescales of a few days followed by a slow decline lasting $\sim$100 days. No periodic pattern is observed in the long-term light curve. Our spectroscopic observations, obtained between JD 2455700 and 2455988, occur during a relatively long phase of quiescence, when the photometric activity, if present, is at the level of $\Delta V \approx 0.02$ mag. Just after the infrared observations, a major outburst started around JD 2456030 lasting around 150 days.

We have analyzed an outburst in order to compare the conclusions obtained by Haubois et al. (2012) with our photometric data. We have chosen an outburst centered in MJD = 56066.22 due to its strength and amplitude of $\Delta V = 0.4$ mag. The outburst was fitted by a fifth-degree polynomial and compared with the models done by Haubois et al. (2012). If we split the outburst at its maximum brightness, which should be where the central star stop feeding the disk, there is a build-up stage and a dissipation stage. We have found the dissipation timescale to be larger than the build-up stage, finding a build-up timescale of 46.4 days and a decay lasting 116.78 days (Figure 1). Their results are in agreement with the predictions by Haubois et al. (2012).

3.2. Line Identification and Line Parameters

We identify emission Hydrogen recombination lines, as the Humphreys lines from transition 14−6 to 30−6 (Table 4). At some epochs, we observe higher-order Humphreys lines. This is due to different conditions of the envelope and can be seen in Lenorzer diagram (5). The higher order observed was Hu(30−6) at dates MJD 55981.2482 and MJD 55988.3589. Also, we identify emission in Brα, Pfγ, Pfϵ, and Pfδ, displayed in Figure 3 as follows: Brα by a black triangle, Pfγ by a gray triangle, and the Humphreys series by white triangles from the transition 14−6 beside Br α to the end of the series. Another identified line in the first spectrum is the line He I 4.038–4.041 μm that disappeared toward the end of the observations. This line was also observed in μ Centauri and other Be stars and related objects—OZ Nor, V4024 Sgr, and V1150 Tau—by Mennickent et al. (2009)—here and after M09—but in those observations, the emission in Pfγ and Pfϵ was not detected.

The spectra shortward of 3.5 μm were not successfully corrected by telluric lines due to high variability of the atmospheric features in this region. Since diagnostic lines used for the analysis are outside this zone, we omitted the problematic region from the analysis. The target lines in this study are the Hydrogen Humphreys series, Brα and Pfγ. The measurement of the main parameters as equivalent width (EW) and full width at
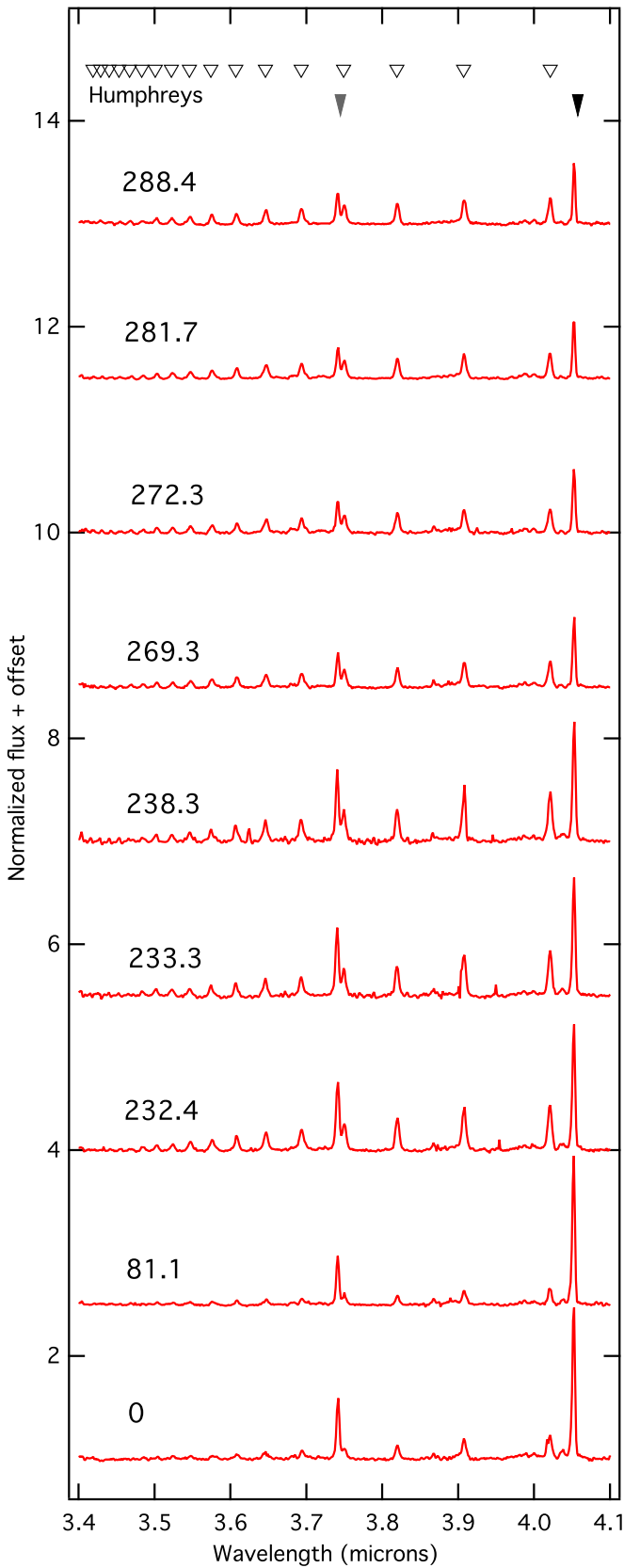

Figure 3. *L*-band spectra of μ Cen, time direction goes upward. The black arrow indicates the position of Brα and gray arrow of Pfγ. The number beside each spectra indicates the number of days from the first spectrum.

Table 3
BSM Photometry for μ Centauri Used for Comparison with Visual Magnitudes

MJD	V	Verr	$B - V$
56094.1326	3.200	0.007	−0.125
56098.1210	3.211	0.006	−0.147
56105.1020	3.298	0.003	−0.168
56106.1003	3.329	0.006	−0.153
56399.2881	3.542	0.002	−0.233
56422.2303	3.437	0.005	−0.234
56436.1932	3.455	0.013	−0.223
56472.1009	3.481	0.032	−0.226
56482.0747	3.463	0.005	−0.262
56483.0723	3.535	0.007	−0.144
56517.9839	3.450	0.018	−0.144

Note. A. Henden (2018, private communication).

Table 4
H I Lines Detected from 3.5 to 4.1 μm in All Observations

λ (μ)	Transition	λ (μ)	Transition
4.052	H I (5−4)	3.546	H I (22−6)
4.021	H I (14−6)	3.522	H I (23−6)
3.907	H I (15−6)	3.501	H I (24−6)
3.819	H I (16−6)	3.483	H I (25−6)
3.749	H I (17−6)	3.467	H I (26−6)
3.740	H I (8−5)	3.453	H I (27−6)
3.693	H I (18−6)	3.440	H I (28−6)
3.646	H I (19−6)	3.429	H I (29−6)
3.607	H I (20−6)	3.419	H I (30−6)
3.574	H I (21−6)	…	…

half maximum (FWHM) were performed using IRAF task splot, and they were measured by fitting a Gaussian to the line profile. The list of the observed lines is presented in Table 4. The values of column densities and relative extension of line forming regions were computed for different lines and epochs and tabulated in Table 5, and nightly parameter reports are given in Tables 6 and 7. The formal error of the fit for the Bracket and Pfund series is 2% in EW and 2.5% in FWHM measurement. For Humphreys, as the line fluxes are lower, the error in the measurement is higher, and we have calculated 6% for EW and 3.5% for FWHM of the emission lines. These errors were estimated by measuring several times the data in order to determine the standard deviation. We are aware that using this technique may underestimate the error. The measured FHWM are related to the true FWHM through the relation

$$\text{FWHM}_{\text{TRUE}} = \sqrt{\text{FWHM}_{\text{OBS}}^2 - \text{FWHM}_{\text{INS}}^2}$$

where FWHM_{INS} is the instrumental FWHM equal to 31 Å.

3.2.1. Equivalent Widths and FWHM Behavior

We present, for the fist time in Figure 4, the evolution for a single star between EW/λ and wavelength for the Humphreys series. There is not a well defined pattern for EW/λ along our time coverage for Humphreys lines; however, there seems to be a trend in the behavior of the Brackett α and Pfund γ lines. In the first observation, there is a large difference between Brα, Pfγ, and Humphreys lines, but when time goes by, EW/λ of

Table 5
Hydrogen Column Densities for Level 6 and Relative Extension of the Forming Regions of Humphreys Lines

λ	55699.9891		55781.0428		55932.3567	
	N_6	$\Delta R_n/\Delta R_{16}$	N_6	$\Delta R_n/\Delta R_{16}$	N_6	$\Delta R_n/\Delta R_{16}$
μm	$10^{14}\,\mathrm{cm}^{-2}$		$10^{14}\,\mathrm{cm}^{-2}$		$10^{14}\,\mathrm{cm}^{-2}$	
4.021	0.68	0.37	1.98	0.59	1.93	1.55
3.907	0.53	0.28	1.52	0.46	0.50	0.40
3.819	1.83	1.00	3.33	1.00	1.25	1.00
3.749	2.38	1.30	2.99	0.90	1.71	1.37
3.693	3.54	1.93	1.77	0.53	1.47	1.18
λ	55933.3129		55938.3051		55969.3290	
	N_6	$\Delta R_n/\Delta R_{16}$	N_6	$\Delta R_n/\Delta R_{16}$	N_6	$\Delta R_n/\Delta R_{16}$
μm	$10^{14}\,\mathrm{cm}^{-2}$		$10^{14}\,\mathrm{cm}^{-2}$		$10^{14}\,\mathrm{cm}^{-2}$	
4.021	1.34	0.86	1.21	0.95	1.35	0.82
3.907	0.35	0.22	0.40	0.31	1.94	1.18
3.819	1.56	1.00	1.28	1.00	1.65	1.00
3.749	1.13	0.72	0.15	0.12	1.10	0.67
3.693	1.95	1.25	1.68	1.32	…	…
λ	55972.3378		55981.2482		55988.3589	
	N_6	$\Delta R_n/\Delta R_{16}$	N_6	$\Delta R_n/\Delta R_{16}$	N_6	$\Delta R_n/\Delta R_{16}$
μm	$10^{14}\,\mathrm{cm}^{-2}$		$10^{14}\,\mathrm{cm}^{-2}$		$10^{14}\,\mathrm{cm}^{-2}$	
4.021	3.01	1.08	3.05	0.91	2.36	0.95
3.907	2.45	0.88	2.51	0.75	2.50	1.01
3.819	2.80	1.00	3.36	1.00	2.49	1.00
3.749	3.18	1.14	3.05	0.91	2.65	1.06
3.693	2.04	0.73	2.16	0.64	1.65	0.66

Table 6
Equivalent Widths in Å, for Hydrogen Recombination Lines Observed

MJD	$EW_{Br\alpha}$	$EW_{Pf\gamma}$	$EW_{Hu_{14}}$	$EW_{Hu_{15}}$	$EW_{Hu_{16}}$	$EW_{Hu_{17}}$	$EW_{Hu_{18}}$	$EW_{Hu_{19}}$	$EW_{Hu_{20}}$	$EW_{Hu_{21}}$
55699.9891	61.1	26.1	16.4	13.4	8.7	6.7	5.1	5.8	4.2	3.7
55781.0428	64.5	23.3	10.2	9.6	6.0	5.4	5.2	4.9	4.0	3.7
55932.3567	55.4	34.2	25.7	30.0	21.2	16.2	13.7	12.7	9.8	8.7
55933.3129	54.3	31.3	27.8	28.5	18.3	15.7	12.0	11.6	9.2	8.3
55938.3051	55.2	33.0	29.7	28.9	19.7	18.3	12.7	11.9	8.9	8.8
55969.3290	29.4	15.9	17.0	12.2	10.8	9.4	9.3	6.7	6.5	5.6
55972.3378	26.8	15.1	15.7	16.2	13.4	10.8	10.4	9.9	6.4	6.3
55981.2482	24.4	14.5	16.0	16.5	12.6	11.3	10.6	10.2	6.6	5.9
55988.3589	25.1	15.7	16.8	14.5	12.7	10.6	9.9	9.3	6.9	6.6
MJD	$EW_{Hu_{22}}$	$EW_{Hu_{23}}$	$EW_{Hu_{24}}$	$EW_{Hu_{25}}$	$EW_{Hu_{26}}$	$EW_{Hu_{27}}$	$EW_{Hu_{28}}$	$EW_{Hu_{29}}$	$EW_{Hu_{30}}$	
55699.9891	2.41	2.50	1.69	1.20	…	…	…	…	…	
55781.0428	3.41	2.04	1.36	…	…	…	…	…	…	
55932.3567	7.31	5.10	3.75	2.66	3.51	2.53	1.25	…	…	
55933.3129	7.96	5.01	4.27	2.35	…	…	…	…	…	
55938.3051	7.16	5.68	4.06	2.36	…	…	…	…	…	
55969.3290	4.49	4.15	2.95	2.21	1.80	1.22	…	…	…	
55972.3378	5.29	3.42	3.21	1.99	1.72	1.30	1.39	1.06	0.91	
55981.2482	5.43	4.10	3.12	2.53	1.81	1.28	1.37	0.98	1.13	
55988.3589	6.65	5.70	4.19	3.44	…	…	…	…	…	

Note. Typical error is 6%.

Brα and Pfγ decrease, eventually reaching values close to those measured for the Humphreys lines. In addition, we observe a break up in the EW values from MJD 55938.3051 to MJD 55969.3290; these are our fifth and sixth observations. Between these two dates, the equivalent width values decrease abruptly. This is observed for all of the lines identified. The analysis of FWHM does not reveal any particular behavior along time.

4. Discussion

4.1. On Emission Line Decrements

We have measured line strengths in order to apply a diagnostic tool presented by Lenorzer et al. (2002b)—here and after L02a—where a diagram of $\log(Hu_{14}/Br_{\alpha})$ versus $\log(Hu_{14}/Pf_{\gamma})$ can be used to test the optical depth conditions

Table 7
Observed FWHM in Å, for Each Hydrogen Recombination Line

MJD	$FWHM_{Br\alpha}$	$FWHM_{Pf\gamma}$	$FWHM_{Hu14}$	$FWHM_{Hu15}$	$FWHM_{Hu16}$	$FWHM_{Hu17}$	$FWHM_{Hu18}$	$FWHM_{Hu19}$	$FWHM_{Hu20}$	$FWHM_{Hu21}$
55699.9891	38.4	42.0	76.8	71.9	60.8	68.4	60.5	95.5	92.5	106.3
55781.0428	41.0	46.1	74.3	70.2	62.3	56.5	53.2	74.4	79.1	71.0
55932.3567	42.0	49.1	57.2	69.2	61.4	59.6	73.1	71.1	64.9	81.9
55933.3129	44.3	46.6	60.6	66.0	59.3	58.2	62.4	69.1	64.1	76.1
55938.3051	44.7	46.2	63.2	66.7	62.6	61.4	68.8	68.0	62.7	80.8
55969.3290	39.0	44.8	68.8	59.6	60.8	70.6	73.9	62.5	76.9	80.9
55972.3378	39.6	45.8	65.7	70.3	64.9	62.3	78.6	75.1	65.8	74.7
55981.2482	37.9	46.2	61.8	69.5	60.2	62.0	76.5	78.9	61.2	69.3
55988.3589	37.3	49.0	62.5	62.0	58.6	55.7	65.42	64.7	61.4	64.6

| MJD	$FWHM_{Hu22}$	$FWHM_{Hu23}$	$FWHM_{Hu24}$	$FWHM_{Hu25}$	$FWHM_{Hu26}$	$FWHM_{Hu27}$	$FWHM_{Hu28}$	$FWHM_{Hu29}$	$FWHM_{Hu30}$
55699.9891	64.5	66.3	53.3	48.7	...	...	...	...	...
55781.0428	95.6	65.4	52.1	...	...	...	...	...	...
55932.3567	79.0	73.0	61.3	67.2	75.6	92.5	61.9	...	...
55933.3129	100.1	72.2	62.3	54.1	...	...	...	...	...
55938.3051	91.6	78.7	59.9	54.2	...	...	...	...	...
55969.3290	79.7	75.0	54.0	60.7	57.5	67.3	...	...	...
55972.3378	72.7	60.9	56.7	67.1	54.0	73.7	45.6	32.4	44.4
55981.2482	76.3	69.8	57.2	63.0	71.8	68.5	98.5	41.6	66.7
55988.3589	74.9	68.6	59.1	...	...	...	...	...	...

Note. Typical error is 3.5%.
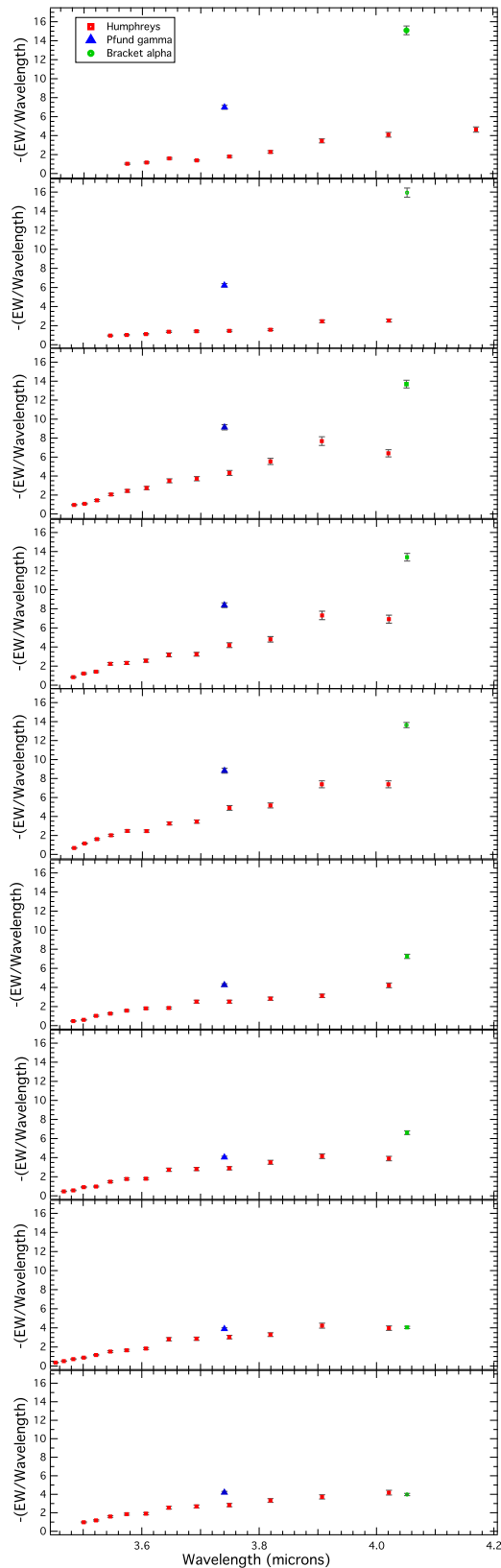
Figure 4. EW/λ vs. wavelength for Brα, Pfγ, and Humphrey lines. The first observation corresponds to the lower frame and time direction goes upwards.

Figure 5. Line flux ratio diagram for $\log(\text{Hu}_{14}/\text{Br}_\alpha)$ vs. $\log(\text{Hu}_{14}/\text{Pf}_\gamma)$, showing the evolution track of μ Centauri during our observations. The black asterisk shows the position for μ Centauri reported by M09, the gray circle denotes the position for an optically thin case, and the dashed box represents the zone for an optically thick condition as reported by L02a.

from an optically thin zone to an optically thick one. Accordingly, the position of μ Centauri during the observation of M09 is near the optically thin region.

The correlation between EW/λ and wavelength in Figure 4 was reported by M09 in 13 Be stars and is also observed in γ Cas (Hony et al. 2000). The change in emission intensities between Pfγ and Brα lines relative to those of Humphreys lines is consistent with a transition from group II to group I according to M09 classification, i.e., a transition from an optically thin to optically thick circumstellar envelope.

Observing the light curve of μ Centauri in Figure 2 (top panel), we do not see large variability of the *V* magnitude during the time span of the observations (the list of visual magnitudes is displayed in Table 8 within the Appendix). However, the *L*-band spectra display a huge variability in the intensity of Humphreys series, Brα, and Pfγ lines. This behavior is reflected in Figures 4 and 5, where the line changes are displayed.

4.2. Estimation of Column Densities and Extension of Line-forming Regions

Following the approximative but insightful procedure presented in Granada et al. (2010), we have estimated atomic column densities and the relative extensions for the forming region of Humphreys lines. For those Humphreys' lines with fluxes that deviate from the ones corresponding to the optically thin case, rough estimates of the atomic column density and the extension of the line-forming regions can be made. Figure 6 shows the line flux ratios for different Humphreys' lines for different epochs together with the theoretical optical thin case (Baker & Menzel 1938).

We see that at all dates, Humphreys lines present a certain degree of departure from the optically thin case. This is also indicated in Figure 6 by the line flux ratio of $\text{Hu}_n/\text{Hu}_{16}$, which is a good indicator of the envelope optical depth (Hamann & Simon 1987;

in a Be star disk (see also M09 and Sabogal et al. 2017). Our measurements illustrated in Figure 5 show that the position of μ Centauri varies along the diagonal of the graph by moving
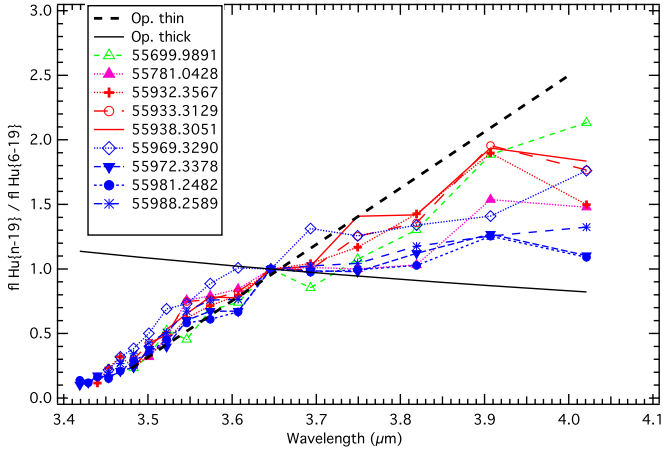
Figure 6. Line flux ratios of Humphreys' lines relative to Hu$_{19}$. Different symbols indicate different epochs. The optically thin case is represented with a dashed straight line, and the optically thick case with a solid line.

Figure 7. Atomic column densities (left), obtained from different lines and epochs: green corresponds to 2011 May 18, pink to 2011 August 08, red from 2012 January 06 to 2012 January 12, and blue from to 2012 February 12 to 2012 March 01.

Hummer & Storey 1987), and theoretically it is found to be close to unity for optically thick envelopes. Thus, we use the following expression to estimate atomic column densities of the lower level of the transition, from different lines,

$$N_i = \ln\left(\frac{\mathrm{Fl}_{\mathrm{Hu}_{nthin}}}{\mathrm{Fl}_{\mathrm{Hu}_n}}\right)\frac{m_e \, c \, \Delta\nu_D}{\sqrt{\pi} \, e^2 \, f_i}, \qquad (1)$$

where m_e and e are the electron mass and charge, respectively, c is the speed of light, f_i is the line oscillator strength, $\mathrm{Fl}_{\mathrm{Hu}_n}$ is the measured flux of the nth Humphreys line, and $\Delta\nu_D$ is the Doppler width of the line in frequency units. Considering that rotation is the main broadening mechanism, the broadening in velocity is taken as $V \sin i = 194 \, \mathrm{km \, s^{-1}}$ (Bernacca & Perinotto 1970).

Since Humphreys lines are formed in the inner regions of the disk and several studies show that volumetric density varies with a lower exponent within three stellar radii (e.g., Zorec et al. 2007), we now consider that volumetric density is constant throughout all Humphreys' line-forming regions. By taking this into account if we observe differences in column densities, those differences are related to changes in the extension of line-forming regions. Then we can obtain the extension of line-forming regions, relative to one of them:

$$\frac{\Delta R_{\mathrm{Hu}_n}}{\Delta R_{\mathrm{Hu}_{16}}} = \frac{\Delta N_{i_{\mathrm{Hu}_n}}}{\Delta N_{i_{\mathrm{Hu}_{16}}}}. \qquad (2)$$

The values of column densities and relative extension of line-forming regions are plotted in Figure 7. We estimate the uncertainty in the determination of N_i is 40%, and 20% for relative extension.

We find that the column densities vary in time within different epochs. In the first observation, the large column density differences with wavelength suggest that the assumption of constant density could be inadequate, because a density gradient in the Humphreys forming region could exist. The fact that the FWHM of Humphreys lines has a wavelength dependency at this epoch supports the conjecture that the line forms in somehow different conditions. In other
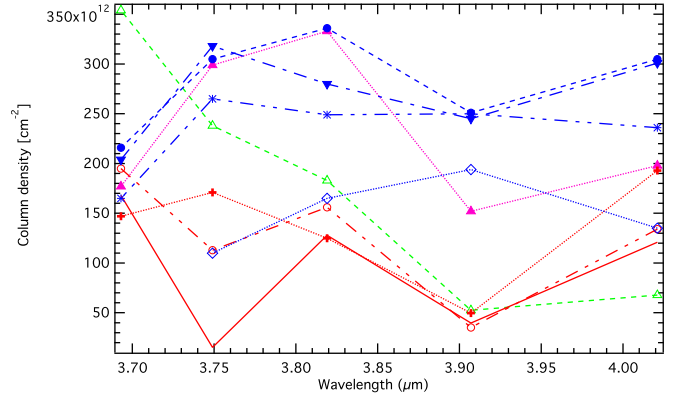
epochs, the column densities exhibit a less dramatic behavior with wavelength (or at least they do not show a clear trend), and the FWHM remains within a smaller range for each observation.

During the last epoch, indicated by blue in our plots, an increase in the column density of $1.5 \times 10^{14} \, \mathrm{cm^{-2}}$ (or an increase in a factor of $\sim$2) occurred in 2 days. Because the rotational conditions of the line-forming region did not change significantly during these two days, we can assume that the variation in column density was due to a change in the (volumetric) density of the medium, or equivalently, due to a variation of the mass in the circumstellar envelope. However, we have to keep in mind that we obtain the column density of hydrogen atoms at level 6 (Humphreys series), so we cannot directly derive the total amount of mass injected. We could imagine though, that whatever the mass in the inner regions of the disk was, it was multiplied by a factor of 2.

4.3. Continuum Variability

We have calculated a flux ratio B_L/R_L where B_L and R_L are blue and red integrated fluxes in L-band zones depleted of emission lines. For that, we have calculated for each epoch the ratio between the spectra of μ Centauri and the standard star HR4903 and then calculated S_λ as this ratio multiplied by a blackbody spectrum of the same temperature that the effective temperature that HR4903. Hence, we obtained a set of spectra whose flux zero point is not constrained but with slopes roughly preserving the characteristics of the original spectra. In these spectra, we calculated the flux ratio as

$$\frac{B_L}{R_L} = \frac{\int_{3.40}^{3.45} S_\lambda \cdot d\lambda}{\int_{3.91}^{3.95} S_\lambda \cdot d\lambda}. \qquad (3)$$

The evolution of B_L/R_L throughout time is displayed in Figure 8 (left). For μ Centauri, this flux ratio turns to be bluer toward the end of the period observed. We observe a reddening in comparison with the expected value for a blackbody radiator with the same temperature that the effective temperature of μ Centauri, and this reddening is in agreement with a disk obscuring the central star.
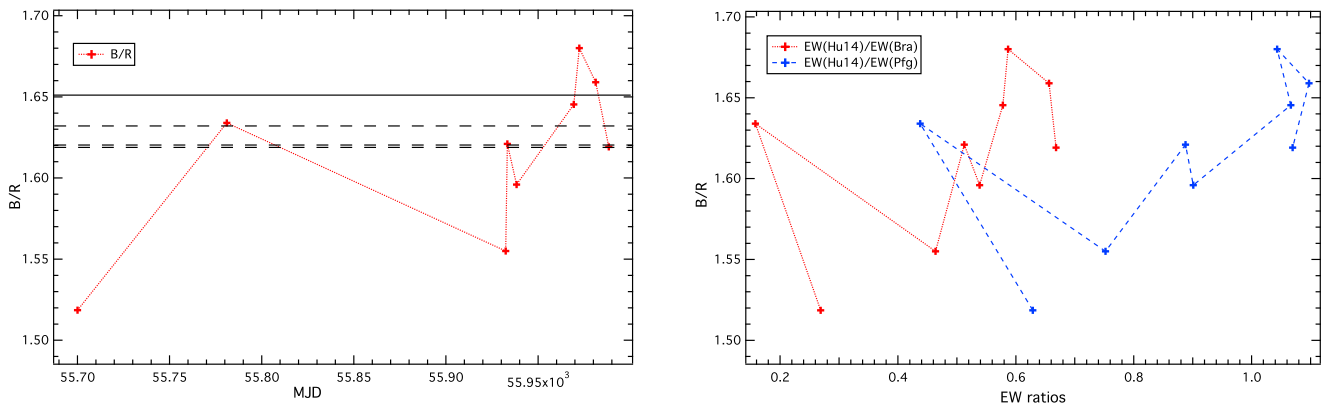
Figure 8. (Left panel) Evolution of the flux ratio described in Equation (3) vs. time, the three horizontal lines are representative of simple blackbody radiators at different effective temperatures: the double dashed line represents $T = 10000$ K, the single dashed line shows $T = 15000$ K, and the solid line represents $T = 22400$ K, which is the effective temperature of μ Centauri. (Right panel) The variation of the flux ratio vs. the decrements $\mathrm{Hu}_{14}/\mathrm{Br}\alpha$ and $\mathrm{Hu}_{14}/\mathrm{Pf}\gamma$ used in the Lenorzer diagram.

The emission lines observed in the L-band and the variation of their strengths indicate that even at optical quiescence there is an active envelope around μ Centauri. Because of the relatively small inclination of this star (Hanuschik 1989), it is expected that the continuum intensity contribution from the central star is the same for all of the observations. Then, the observed variability between epochs is rather linked to circumstellar disk changes.

We find an overall increase in B_L/R_L, which means the spectra become bluer toward the end of our near-IR spectroscopic campaign. The global tendency of B_L/R_L increasing before a major outburst, or equivalently the reduction of disk continuum emission, in coincidence with the presence of more compact and optically thick L-band hydrogen line emitting regions, could be an indication of a precursor stage, similar to the cycle of slow recovery to the quiescence magnitude prior to outburst, as described by Rivinius et al. (1998a) and as expected for a star about to start developing a CMD loop due to disk build-up (de Wit et al. 2006). Unfortunately, our time sampling is too limited to provide a precise temporal behavior of the system.

The use of the L-band can be an excellent tool in the study Be star disks, and we expect that fully covering an outburst episode would provide significant insight into the Be phenomenon.

5. Conclusions

We have performed for the first time a multi-epoch spectroscopic monitoring of a Be star in the L-band region of the near-IR, which is particularly sensitive to physical conditions of the innermost region of circumstellar envelope. We report these observations of the Be star μ Centauri together with long-term visual photometry, showing relatively frequent outburst episodes that are non-periodic and stochastic in nature, over 16 years. Even when the V magnitude remained

practically at a constant level or without significant changes in brightness during almost one year of our spectroscopic observations, we do observe considerable variability in the intensity of H I recombination lines sensitive to optical depth changes. These changes are consistent with the transition from an optically thin to an optically thick stage observed toward the end of our spectroscopic observing campaign. We also analyzed the near-IR continuum slope variability, finding that the system is bluer when the line emission is optically thick, preceding the major outburst. Because of the gap of a couple of weeks between our near-IR observations and the detection of the outburst, we cannot affirm that the observed changes in our near-IR spectra and the major outburst are causally connected. However, if they were indeed connected, our IR spectra would be the first observations of a disk building phase in the L-band. Moreover, because these observations trace the changes of the innermost disk regions close to the star, these changes would correspond to very early epochs in the disk build-up. Certainly, new multi-epoch and multi-wavelength monitoring of μ Centauri and other Be stars, together with detailed line modeling, are necessary to understand the disk build-up process.

Appendix
Photometry Tables

Table 8
Visual Photometry for μ Centauri

MJD	Visual Magnitude (mag.)	Visual Error (mag.)
50537.7080	3.270	0.10
50558.6900	3.310	0.08
50564.6800	3.350	0.08
50608.6041	3.290	0.08
50609.6666	3.300	0.08

(This table is available in its entirety in machine-readable form.)

ORCID iDs

G. Aguayo ⓘ https://orcid.org/0000-0003-1784-7200

References

Argelander, F. W. A. 1843, (Berlin: S. Schropp) XIX, 119 ; in 8.; DCCC.8.6,
Baade, D. 1984, A&A, 135, 101
Baker, J. G., & Menzel, D. H. 1938, ApJ, 88, 52
Balona, L. A., James, D. J., Lawson, W. A., & Shobbrook, R. R. 2001, MNRAS, 324, 1041
Bernacca, P. L., & Perinotto, M. 1970, CoAsi, 239, 1
Bjorkman, J. E. 1997, in Stellar Atmospheres: Theory and Observations, ed. J. P. De Greve, R. Blomme, & H. Hensberge (Berlin: Springer), 239
Bjorkman, J. E., & Carciofi, A. C. 2005, in The Nature and Evolution of Disks Around Hot Stars 337, 75
Carciofi, A. C., Bjorkman, J. E., Otero, S. A., et al. 2012, ApJL, 744, L15
Chesneau, O., Meilland, A., Chapellier, E., et al. 2014, A&A, 563, A71
Chojnowski, S. D., Whelan, D. G., Wisniewski, J. P., et al. 2015, AJ, 149, 7
Chojnowski, S. D., Wisniewski, J. P., Whelan, D. G., et al. 2017, AJ, 153, 174
Cuypers, J., Balona, L. A., & Marang, F. 1989, A&AS, 81, 151
Dachs, J., Kiehling, R., & Engels, D. 1988, A&A, 194, 167
de Wit, W. J., Lamers, H. J. G. L. M., Marquette, J. B., & Beaulieu, J. P. 2006, A&A, 456, 1027
Dougherty, S. M., Waters, L. B. F. M., Burki, G., et al. 1994, A&A, 290, 609
Draper, Z. H., Wisniewski, J. P., Bjorkman, K. S., et al. 2014, ApJ, 786, 120
Feinstein, A. 1968, ZA, 68, 29
Feinstein, A. 1975, PASP, 87, 603
Frémat, Y., Zorec, J., Hubert, A.-M., & Floquet, M. 2005, A&A, 440, 305
Granada, A., Arias, M. L., & Cidale, L. S. 2010, AJ, 139, 1983
Gutierrez-Moreno, A., & Moreno, H. 1968, ApJS, 15, 459

Hamann, F., & Simon, M. 1987, ApJ, 318, 356
Hanuschik, R. W. 1989, ApJS, 161, 61
Hanuschik, R. W., Dachs, J., Baudzus, M., & Thimm, G. 1993, A&A, 274, 356
Harmanec, P. 1983, HvaOB, 7, 55
Harmanec, P. 1987, IBVS, 3097, 1
Haubois, X., Carciofi, A. C., Rivinius, T., Okazaki, A. T., & Bjorkman, J. E. 2012, ApJ, 756, 156
Haubois, X., Mota, B. C., Carciofi, A. C., et al. 2014, ApJ, 785, 12
Hony, S., Waters, L. B. F. M., Zaal, P. A., et al. 2000, A&A, 355, 187
Hummer, D. G., & Storey, P. J. 1987, MNRAS, 224, 801
Jaschek, M., Slettebak, A., & Jaschek, C. 1981, BeSN, 4, 9
Jones, C. E., Molak, A., Sigut, T. A. A., et al. 2009, MNRAS, 392, 383
Labadie-Bartz, J., Chojnowski, S. D., Whelan, D. G., et al. 2017, arXiv:1708.02594
Lee, U., Osaki, Y., & Saio, H. 1991, MNRAS, 250, 432
Lenorzer, A., de Koter, A., & Waters, L. B. F. M. 2002a, A&A, 386, L5
Lenorzer, A., Vandenbussche, B., Morris, P., et al. 2002b, A&A, 384, 473
Maiolino, R., Rieke, G. H., & Rieke, M. J. 1996, AJ, 111, 537
Marlborough, J. M., Zijlstra, J.-W., & Waters, L. B. F. M. 1997, A&A, 321, 867
Martayan, C., Frémat, Y., Hubert, A.-M., et al. 2007, A&A, 462, 683
Mendoza, V. E. E. 1958, ApJ, 128, 207
Mennickent, R. E., Sabogal, B., Granada, A., & Cidale, L. 2009, PASP, 121, 125
Moorwood, A., Cuby, J.-G., Biereichel, P., et al. 1998, Msngr, 94, 7
Okazaki, A. T., Bate, M. R., Ogilvie, G. I., & Pringle, J. E. 2002, MNRAS, 337, 967
Otero, S., Fraser, B., & Lloyd, C. 2001, IBVS, 5026, 1
Otero, S. A., & Moon, T. 2006, JAVSO, 34, 156
Percy, J. R., Jakate, S. M., & Matthews, J. M. 1981, AJ, 86, 53
Perryman, M. A. C., Lindegren, L., Kovalevsky, J., et al. 1997, A&A, 323, L49
Porter, J. M. 1999, A&A, 348, 512
Porter, J. M., & Rivinius, T. 2003, PASP, 115, 1153
Rímulo, L. R., Carciofi, A. C., Rivinius, T., & Haubois, X. 2015, in IAU Symp. Vol. 307, New windows on massive stars: asteroseismology, interferometry, and spectropolarimetry (Cambridge: Cambridge Univ. Press), 133
Rivinius, T., Baade, D., Stefl, S., et al. 1998a, A&A, 333, 125
Rivinius, T., Baade, D., Stefl, S., et al. 1998b, A&A, 336, 177
Rivinius, T., Baade, D., Štefl, S., et al. 2001, A&A, 369, 1058
Rivinius, T., Carciofi, A. C., & Martayan, C. 2013, A&ARv, 21, 69
Sabogal, B. E., Ubaque, K. Y., García-Varela, A., Álvarez, M., & Salas, L. 2017, PASP, 129, 014203
Sigut, T. A. A., & Patel, P. 2013, ApJ, 765, 41
Stagg, C. 1987, MNRAS, 227, 213
Štefl, S., Baade, D., Rivinius, T., et al. 2003, A&A, 402, 253
Townsend, R. H. D., Owocki, S. P., & Howarth, I. D. 2004, MNRAS, 350, 189
Vieira, R. G., Carciofi, A. C., Bjorkman, J. E., et al. 2017, MNRAS, 464, 3071
Zorec, J., Arias, M. L., Cidale, L., & Ringuelet, A. E. 2007, A&A, 470, 239